ACS OMEGA

Open Access

http://pubs.acs.org/journal/acsodf

Article

A Redox-Sensitive Green Fluorescent Protein (roGFP) Sensing Strategy for Dynamic Analysis of Metal Oxide Nanoparticle-Induced Oxidative Stress

Yizhu Wang,[#] Rui Ju,[#] Yan Fu,[#] Fengqi Zhang, Ziyue Yin, Mengyuan Lv, Yanbo Zhu, Zhiqiang Song, Xiaonan Li,* and Na Wang*

Cite This: *ACS Omega* 2025, 10, 15587−15597

Read Online

ACCESS | Metrics & More | Article Recommendations | Supporting Information

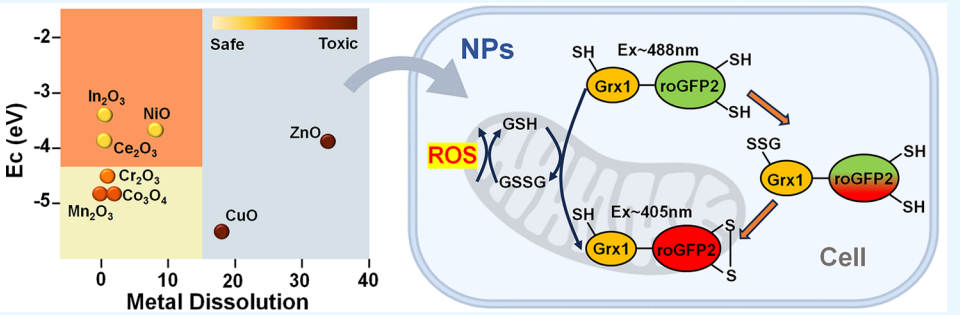

ABSTRACT: The induction of oxygen radicals and oxidative stress are major pathways through which nanomaterials cause adverse health effects. Dynamic monitoring of redox processes in living cells exposed to nanomaterials is currently limited due to the inadequacy of conventional methods. Herein, we construct a Grx1-roGFP2 (glutaredoxin 1 fused with redox-sensitive Green Fluorescent Protein 2) protein sensor expressed in Madin-Darby Canine Kidney (MDCK) cells that allows dynamic analysis of metal oxide (MOx) nanoparticle-induced oxidative stress. We selected eight representative MOx as test objects, ranking their toxicity potentials according to the overlap degree of their band gap energies with cellular redox potentials and their ability to release metal ions to catalyze the generation of oxygen radicals. The sensor demonstrates high sensitivity in detecting MOx-induced intracellular redox fluctuations, operating within a 6−200 mg/mL range and a 30-min response time, while maintaining sustained sensitivity over 24 h. The sensor utilizes an oxidation/reduction ratio curve to precisely characterize the unique pattern of oxidative stress induced by each MOx, encompassing the stress's intensity (curve slope), amplitude (curve plateau), features (curve shape), and accumulation of oxygen radicals (curve area integral). These results highlight that the developed Grx1-roGFP2 sensor holds more advantages over traditional probes, showing extensive application prospects in higher standards of nanotoxicological evaluation.

1. INTRODUCTION

The expanding application fields and commercial production of artificial nanomaterials have continuously intensified people's emphasis on the toxicological aspects of nanomaterials.[1−3] Metal oxide (MOx) nanoparticles constitute a significant class of nanomaterials, and the semiconducting characteristics of MOx nanoparticles make them valuable as catalysts in both engineered and natural redox reactions.[4,5] However, throughout their lifecycle, from synthesis to application and eventual disposal, MOx nanoparticles pose potential public health risks, necessitating sensitive nanotoxicological assessments to manage them and safeguard human health.[6−8] In contrast to traditional toxicological studies that emphasize dosage, chemical composition, and exposure pathways, nanotoxicology testing requires additional consideration of the distinctive physicochemical properties of nanoparticles, encompassing size effects, quantum effects, ultralarge area-to-volume ratio, and high reactivity.[9−11] Thus, complex nanotoxicological effects are in urgent need of a comprehensive and authoritative evaluation system.

The induction of oxygen radicals and oxidative stress by MOx nanoparticles is the principal route through which they have adverse impacts on health.[7,12,13] For the multimembered MOx family, Burello and Worth proposed a theoretical framework linking cellular redox potential to MOx band gaps to explain the oxidative stress and toxicity of certain materials.[14,15] This band gap hypothesis suggests that the oxidative stress potential of MOx nanoparticles can be

Received: January 25, 2025
Revised: March 27, 2025
Accepted: March 28, 2025
Published: April 9, 2025

predicted by comparing their band gap energies to the cellular redox potential. When biological and material energy states align, electron transfer is likely to occur, interfere with the antioxidant system, facilitate the generation of reactive oxygen species (ROS), and trigger oxidative stress. Beyond the potential role of surface energy states of MOx nanoparticles, it is crucial to account for the impact of particle dissolution and metal ion release on their toxicity.[16,17] The propensity for dissolution is governed by the solubility of the metal in the specific biological milieu and the concentration gradient from the particle surface to the surrounding solution. In the case of highly soluble materials such as ZnO and CuO nanoparticles, their primary toxicological concern stems from the liberation of metal ions.[18,19] However, for materials with lower solubility, both the catalytic activity of the nanoparticle surface and the release of ions may contribute to toxicity and the production of ROS. Therefore, the determination of ROS is gradually becoming an important indicator for evaluating the toxicity of MOx.

Determination of oxygen radicals currently relies on two principal methodologies: indirect assessment of redox markers, such as NADPH, ascorbic acid, and GSH, through techniques like HPLC or gel electrophoresis; and direct ROS detection, which includes fluorescent probes and electron spin resonance methods.[20−22] Indirect methods risk artifactual oxidative damage due to cell disruption and extraction processes. Direct detection, while less invasive, is prone to interference from substrate absorption and cell permeability issues, and fluorescent reagents may introduce cytotoxicity and irreversibility concerns, limiting their *in vivo* application.[23,24] Consequently, to enhance specificity and reduce nonspecific interactions in complex biological systems, developing targeted probes to achieve real-time and dynamic monitoring of ROS constitutes a practical requirement for nanotoxicological evaluation and mechanism exploration.

Recent advances in redox-sensitive GFP (roGFP) probes have achieved the goal of monitoring ROS at a subcellular resolution level.[25,26] The roGFP probes contain an engineered dithiol/disulfide switch on their surface that can sense redox equilibrium by measuring the change in fluorescence ratio converted by the engineered switch.[26] The glutathione redox pair (GSH/GSSG) and hydrogen peroxide (H_2O_2) are crucial links in redox homeostasis and redox signaling.[27,28] Importantly, roGFP2 can be directly fused to glutaredoxin (Grx), thereby increasing the specificity of glutathione redox potential measurements. Advances in gene editing technology have made it possible for fused Grx-roGFP2 to monitor redox homeostasis under different scenarios, such as cell types, subcellular compartments, developmental stages, and environmental conditions.[26,29−31] Similarly, roGFP can also be coupled with multiple enzymes involved in the antioxidant system to fabricate diverse reactive oxygen species probes,[32,33] e.g., roGFP is coupled with peroxidase 1 (Orp1) to become a H_2O_2-specific probe.[34] Thus, the roGFP-based probes show great potential in nanotoxicological assessments involving oxidative stress.

Herein, we develop a Grx1-roGFP2 fusion protein sensor expressed in MDCK cells, which enables the fluorescence switch of the oxidized/reduced state of the roGFP2 protein through the transfer of Grx1 disulfide bonds during the redox process. With the aid of a high-content cell imaging system, this sensor enables real-time dynamic monitoring of fluctuations in glutathione redox potential in living cells. We selected eight representative MOx with different band gap energies and metal ion solubilities as test objects. Thus, we employed the constructed Grx1-roGFP2 sensor to assess the oxidative stress induced by the different MOx nanoparticles. By mapping the fluorescence ratio signal, we monitored the response performance of the sensor under exposure to different MOx nanoparticles, thereby obtaining the unique profile of oxidative stress induced by each MOx nanoparticle. In short, the developed Grx1-roGFP2 sensor offers a feasible and effective strategy for nanotoxicological assessment.

2. MATERIALS AND METHODS

2.1. Materials. MOx nanoparticles were purchased from UG. NANO (Suzhou, China). Anti-Bax polyclonal antibody, Anti-Bcl2 polyclonal antibody, and β-actin polyclonal antibody were purchased from Bioss (Beijing, China). Madin-Darby canine kidney (MDCK) cells were purchased from the Institute of Materia Medica, Chinese Academy of Medical Sciences, Beijing. Dulbecco's Modified Eagle's Medium (DMEM), penicillin−streptomycin, and fetal bovine serum (FBS) were sourced from GIBCO, Invitrogen Corp. (Carlsbad, CA, USA). The FITC-Annexin V Apoptosis Detection Kit was purchased from BD Biosciences (New York, USA). The CM-H_2DCFDA Assay Kit was purchased from MACKLIN (Shanghai, China). The MTS tetrazolium compound was purchased from Promega Corp. (Madison, WI, USA). All other reagents were of analytical grade from commercial sources.

2.2. Cell Culture. MDCK cells were cultured in 25 cm^2 cell culture with DMEM supplemented with 10% FBS and streptomycin-penicillin (100 μg/mL and 100 U/mL, respectively) at 37 °C in a humidified atmosphere of 5% CO_2. Cells were passaged at 70−90% confluency using 0.25% (w/v) trypsin-0.02% (w/v) EDTA solution.

2.3. Construction of pLV-Grx1-roGFP2 Lentiviral Vector. The pLV-Grx1-roGFP2 lentiviral vector was constructed to achieve overexpression of the GRX1-roGFP2 gene. The Grx1-roGFP2 gene coding sequence (CDS) was amplified using polymerase chain reaction (PCR) with specific primers designed to introduce restriction sites *Mlu* I and *Not* I, as well as a Kozak sequence to enhance gene expression. The primer sequences were as follows: Grx1-roGFP2-F: 5′-AATTACGCGTGCCACCATGGCCTC-CACTCGTGTCCTCGCCTC-3′ and Grx1-roGFP2-R: 5′-TTAAGCGGCCGCTCACTTGTACAGCTCGTC-CATGCCGAGAGT-3′. The PCR product was then double-digested with *Mlu* I and *Not* I, and ligated into the pLV-puro vector that had been predigested with the same enzymes. The ligation mixture was transformed into DH5α competent cells and plated on LB agar plates containing ampicillin for selection. Positive clones were identified by PCR using primers as follows: pEGFP-N-5′: 5′-TGGGAGGTCTATATAAGCA-GAG-3′ and PGK-R: 5′-GGAGGAGTAGAAGGTGGCG-3′, and subsequently confirmed by sequencing at Zhongmei Taihe Company.

2.4. Construction of the Grx1-roGFP2 Sensor. The pLV-Grx1-roGFP2 plasmid was extracted from bacterial cultures using a Qiagen Plasmid Plus Midi Kit (QIAGEN, Germany), and its concentration was determined using a UV spectrophotometer. Furthermore, HEK293V cells were seeded in 35 mm dishes. Upon reaching 90−95% confluence, HEK293V cells were transfected with the pLV-Grx1-roGFP2 vector along with packaging plasmids at pH1 and pH2. The cell culture supernatant was collected 48 h post-transfection,

https://doi.org/10.1021/acsomega.5c00774
ACS Omega 2025, 10, 15587−15597

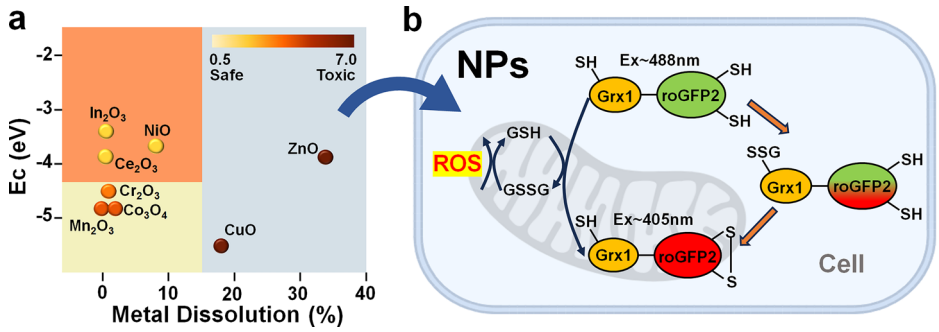

Figure 1. Diagram illustrating the principle of Grx1-roGFP2 sensor for oxidative stress induced by MOx. (a) The selected representative MOx nanoparticles based on their band gap energies and dissolution. (b) Fusion of Grx1 with roGFP2 (Grx1-roGFP2) ensured specificity and rapidity of thiol−disulfide exchange between roGFP2 dithiol and GSH/GSSG pair.

filtered to remove cell debris, and the virus was purified using the PEG lentiviral purification kit. Subsequently, MDCK cells were infected with the lentiviral suspension and incubated for 24 h. Following infection, cells were trypsinized and seeded into 96-well plates with puromycin at a final concentration of 2 μg/mL to select monoclonal cells. Total RNA was extracted from the cells, reverse transcribed, and real-time PCR was performed to quantify the expression of the Grx1-roGFP2 gene using the following primers: Grx1-roGFP2-qF: 5′-GTAAACGGCCACAAGTTCAGCG-3′ and Grx1-roGFP2-qR: 5′-AGGTCAGGGTGGTCACGAGGGT-3′. The expression levels were normalized to the housekeeping gene GAPDH using the following primers: GAPDH-qF: 5′-ATGTTTGTGATGGGCGTGAACC-3′ and GAPDH-qR: 5′-CGGTCTTCTGGGTGGCAGTGAT-3′.

2.5. Performance Evaluation of the Grx1-roGFP2 Sensor. The PE Operetta high-content cell imaging system (PerkinElmer, USA) was employed to assess the performance of the Grx1-roGFP2 sensor in measuring oxidative stress from H_2O_2 treatment. MDCK cells expressing the Grx1-roGFP2 sensor were added with 30 μM H_2O_2, and images were collected at 30-minute intervals for the remaining 24 h. The Grx1-roGFP2 biosensor was excited sequentially at 405 and 488 nm wavelengths, with emission light collected using a 525/30-nm bandpass filter for each excitation. Consistent laser power and pixel dwell time settings were applied across all experiments, while gain adjustments were optimized for each specific trial. Regions of interest (ROIs) were identified and circumscribed around randomly selected individual cells within the field of view. Throughout each experiment, a consistent set of 9 ROIs was monitored. To compare the Grx1-roGFP2 sensor with traditional ROS probes, wild-type MDCK cells were exposed to 30 μM H_2O_2, and fluorescence was measured at desired time using a commercial ROS Assay Kit with CM-H2DCFDA.

2.6. Characterization of MOx Nanoparticles. Eight MOx nanoparticles (ZnO, CuO, NiO, CeO_2, In_2O_3, Mn_2O_3, Co_3O_4, and Cr_2O_3) were selected based on their band gap energies and solubility. All MOx nanoparticles were provided in powdered form. Transmission electron microscopy (TEM, FEI Tecnai G2 T20 U-Twin, USA) was used to observe the nanoparticles' shapes and primary sizes. Samples were prepared by placing a drop of aqueous nanoparticle suspension onto a carbon-coated TEM grid and dried naturally. Hydrodynamic diameters and zeta potential of MOx in various media were measured using a Zetasizer Nano ZS Malvern (Worcestershire, U.K.), and all measurements were carried out at 25 °C.

2.7. Application of the Grx1-roGFP2 Sensor for MOx-Induced Oxidative Stress. MDCK cells expressing the Grx1-roGFP2 sensor were cultured in 96-well plates and allowed to reach a confluence of 70%. Subsequently, the cells were subjected to an incubation period with six distinct concentrations (6, 12, 25, 50, 100, and 200 mg/mL) of MOx nanoparticles for a duration of 24 h. The PE Operetta high-content cell imaging system was employed to capture images and record fluorescence values at intervals of every 30 min. The HCS parameters were standardized as per the experimental protocol previously established,[35,36] ensuring consistency and reliability in data acquisition.

2.8. Cell Viability Assay. The colorimetric MTS assay was employed to assess MDCK cell viability in the presence of the MOx nanoparticles. MDCK cells, seeded at a density of 5×10^5 cells/mL, were exposed to varying concentrations of MOx nanoparticles (6, 12, 25, 50, 100, and 200 mg/mL) and cultured in 96-well plates for durations of 6, 12, and 24 h. After treatment, the medium was aspirated, and the wells were gently rinsed with phosphate-buffered saline (PBS), then 10 μL of 5 mg/mL MTS solution (PBS) was added to each well and incubated for another 4 h at 37 °C. Cell survival relative to control wells was calculated by measuring the absorbance at 570 nm using a microplate reader.

2.9. Cell Apoptosis Assay. Cell apoptosis was performed using the Annexin V-FITC Apoptosis Detection Kit. Wild-type MDCK cells were seeded in six-well plates at a density of 1×10^5 cells per well and allowed to reach 70−80% confluence. The cells were then exposed to varying concentrations of MOx nanoparticles (6, 12, 25, 50, 100, and 200 mg/mL) for 6, 12, and 24 h. Cells were harvested and washed three times with cold PBS, then resuspended in 200 μL of binding buffer and incubated with 10 μL of Annexin V-FITC in the dark at 37 °C for 15 min. Subsequently, 5 μL of PI in 300 μL of binding buffer was added to stain the cells, and flow cytometry was employed for the analysis of stained cells.

2.10. Western Blot Analysis. Expression of apoptosis-related marker proteins was analyzed by western blotting (WB) after the treatment of MDCK cells with MOx nanoparticles. MDCK cells were pretreated with 100 mg/mL of different MOx nanoparticles for 24 h in serum-free DMEM. The cells were lysed in a buffer containing protease inhibitors to prevent degradation, and the total protein concentration was quantified by using the bicinchoninic acid (BCA) assay. Electrophoresis was implemented using 12% (w/v) SDS-

https://doi.org/10.1021/acsomega.5c00774
ACS Omega 2025, 10, 15587−15597

Table 1. Sizes of MOx Nanoparticles in Experimental Dispersion Conditions

MOx	Primary	Water	DMEM	MEM + 10%FBS
Mn_2O_3	46.8 ± 12.9	275.8 ± 8.0	283.9 ± 16.4	299.3 ± 15.1
CuO	22.5 ± 9.2	279.0 ± 8.5	266.2 ± 6.5	292.5 ± 4.1
ZnO	19.8 ± 6.7	214.2 ± 21.6	263.6 ± 9.0	281.2 ± 17.5
Cr_2O_3	78.9 ± 20.2	273.8 ± 14.8	264.9 ± 8.8	299.0 ± 8.7
NiO	10.1 ± 3.7	257.7 ± 9.4	280.3 ± 9.0	296.1 ± 28.8
CeO_2	56.2 ± 27.2	239.1 ± 16.5	241.6 ± 7.9	267.4 ± 3.2
Co_3O_4	22.6 ± 13.1	268.8 ± 15.5	268.3 ± 13.9	290.2 ± 10.3
In_2O_3	52.1± 20.6	241.1 ± 33.3	234.9 ± 7.6	278.2 ± 11.9

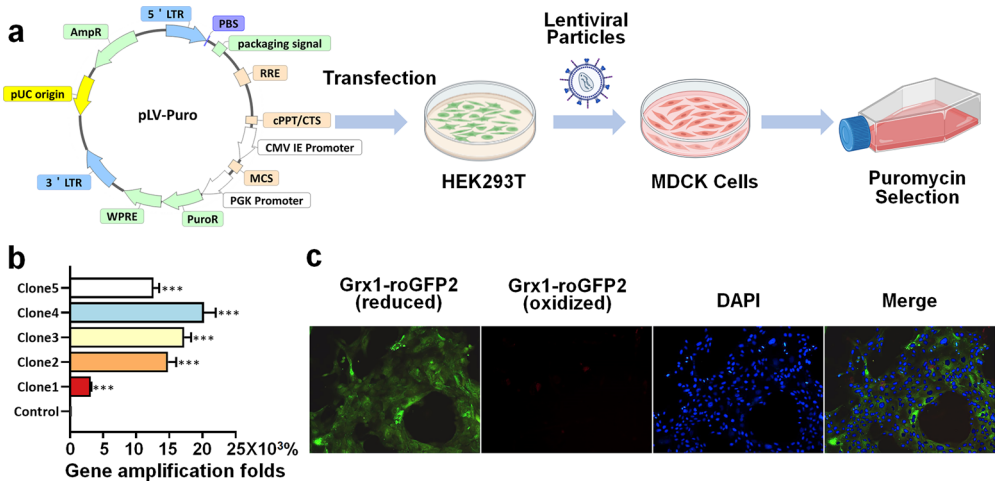

Figure 2. Construction of the engineered MDCK cell line expressing Grx1-roGFP2 sensor. (a) Schematic procedure of preparing stable transfected MDCK cell lines using lentiviral vector. (b) The expression levels of Grx1-roGFP2 fusion gene in screened engineered MDCK cells quantified by qPCR. (c) Fluorescence imaging of the engineered MDCK cells, where green fluorescence indicated the reduced Grx1-roGFP2 sensor and red fluorescence indicated the oxidized Grx1-roGFP2 sensor.

PAGE and then transferred to PVDF membranes (Roche, USA). Densitometric analysis was performed with ImageJ software (v1.8.0).

2.11. Statistical Analysis. The data are expressed as the mean ± standard deviation (SD), and all values were obtained from at least three independent experiments. Statistical significance was evaluated using the Student's *t* test.

3. RESULTS

3.1. Design of the Grx1-roGFP2 Sensor. The construction of the Grx1-roGFP2 sensor and its principle of sensing oxidative stress induced by MOx nanoparticles are schematically illustrated in Figure 1. Herein, eight representative MOx nanoparticles (ZnO, CuO, NiO, CeO_2, In_2O_3, Mn_2O_3, Co_3O_4, and Cr_2O_3), which exhibit a spectrum of band gaps and varying levels of metal dissolution, were selected to evaluate the sensing performance of the developed Grx1-roGFP2 sensor (Figure 1a). Six MOx nanoparticles (NiO, CeO_2, In_2O_3, Mn_2O_3, Co_3O_4, and Cr_2O_3) were specifically chosen based on their ability to engage in electron transfer processes with biological redox couples (−4.12 to −4.84 eV), which are essential for cellular homeostasis.[15] In addition, ZnO and CuO were included in the evaluation due to the recognition that solubility is a key determinant of the toxicity of MOx, independent of energy band structure.

For the Grx1-roGFP2 sensor design (Figure 1b), roGFP2 contains two engineered cysteine residues that can form a reversible disulfide bond. The reduced and oxidized states of roGFP exhibit maximum excitation wavelengths at 488 and 405 nm, respectively, which are determined by their distinct protonation tendencies. Grx1 catalyzes the reaction between roGFP2 and the glutathione redox couple (GSH/GSSG) via thiol−disulfide exchange reactions. The sensing efficiency of roGFP2 alone is limited because its equilibration with the cellular redox system is too slow and lacks selectivity. Thus, the sensor prepared by fusing Grx1 with roGFP2 (Grx1-roGFP2) can significantly improve the specificity and rapid thiol−disulfide exchange rate between roGFP2 and GSH/GSSG conjugates.[26] Consequently, the developed Grx1-roGFP2 sensor allows dynamic live imaging of the glutathione redox potential (E_{GSH}) with high sensitivity and temporal resolution. The sensor's response to redox equilibrium impairment is achieved by calculating the fluorescence ratio in the channel (520 nm), excited with 405 nm (oxidized Grx1-roGFP2) and 488 nm (reduced Grx1-roGFP2) lasers in MDCK cells.

3.2. Characterization of MOx Nanoparticles. TEM analysis provides high-resolution nanoscale images of the eight MOx nanoparticles, revealing their size, shape, and surface structural characteristics (Figure S1). DLS analyses revealed the hydrodynamic sizes of the eight MOx nanoparticles in three different media: water, DMEM, and DMEM supplemented with 10% FBS (Table 1). The results indicated that all nanoparticles exhibited hydrodynamic diameters below 300 nm. Notably, the nanoparticle size in the DMEM medium enriched with 10% FBS was slightly larger compared to those in the other two conditions, which was attributed to the adsorption of the protein corona. The primary sizes of MOx nanoparticles exhibited significant discrepancies compared to

https://doi.org/10.1021/acsomega.5c00774
ACS Omega 2025, 10, 15587−15597

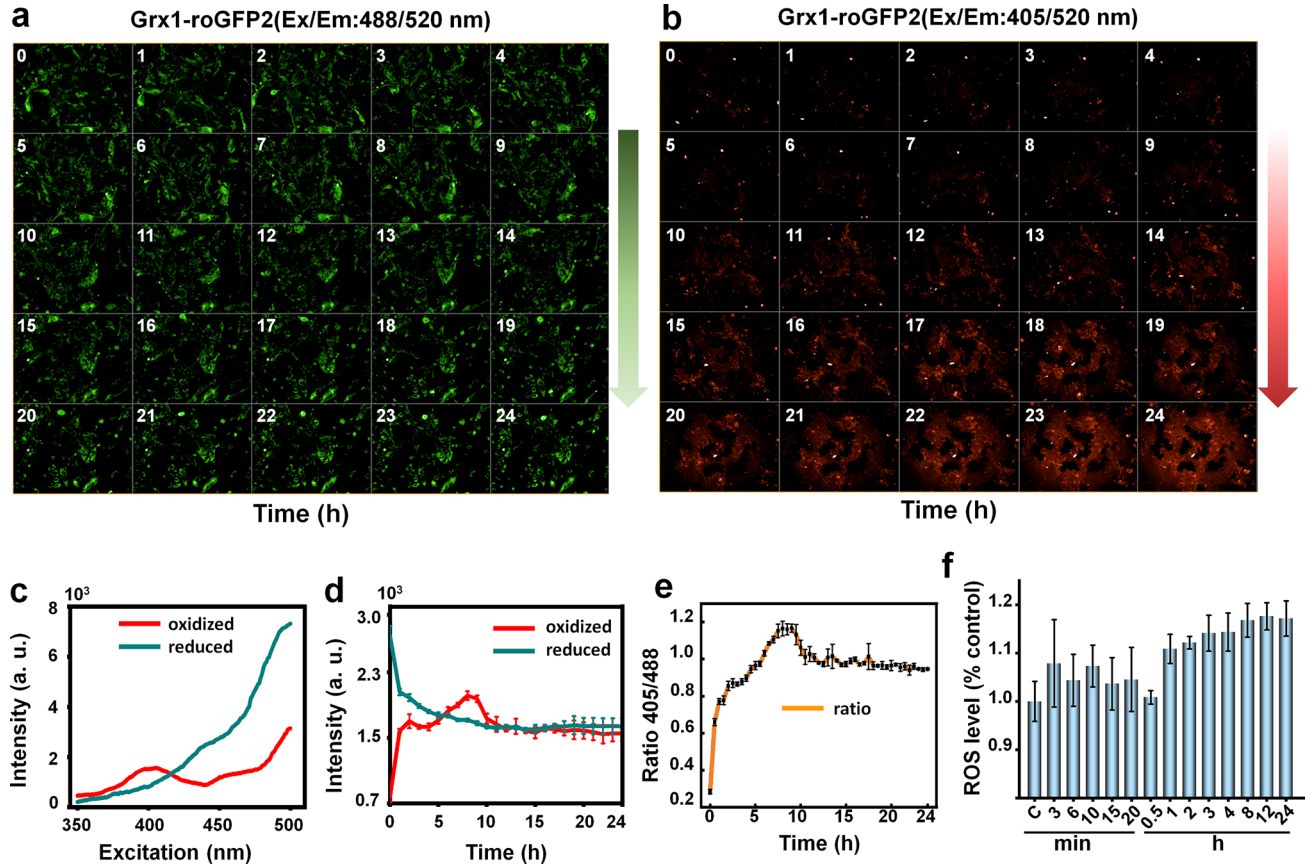

Figure 3. Performance evaluation of the Grx1-roGFP2 sensor in response to H_2O_2 exposure. MDCK cells expressing Grx1-roGFP2 sensor were treated with 30 μM H_2O_2 and monitored continuously for 24 h. (a) The fluorescence images of MDCK cells expressing Grx1-roGFP2 were captured with 488/520 nm used as excitation/emission wavelengths (Ex/Em). (b) The fluorescence images of MDCK cells expressing Grx1-roGFP2 were captured with 405/520 nm used as Ex/Em wavelengths. (c) The excitation spectra of Grx1-roGFP2 in its reduced and H_2O_2-induced oxidized states. (d) fluorescence intensities under 405 and 488 nm excitation. (e) The ratio of 405/488 nm fluorescence intensities, representing the oxidized (red) to reduced (green) states, was calculated from the average fluorescence intensity of all ROIs. (f) Wild-type MDCK cells were treated with 30 μM H_2O_2, and ROS levels were quantified at desired time using CM-H_2DCFDA assay.

their hydrated counterparts, with dimensional variations ranging from several-fold to several dozen-fold. These pronounced size disparities are hypothesized to correlate with the dispersion characteristics of these nanomaterials in aqueous solutions, a phenomenon that has received empirical validation through systematic literature review.[15,37,38] Furthermore, the zeta potential analysis demonstrated that these MOx nanoparticles predominantly bear a negative surface charge (Table S1). Compared with the heterogeneous distribution in water, the zeta potential of MOx exhibited more uniform profiles in both DMEM and DMEM containing 10% FBS.

3.3. Construction of the Grx1-roGFP2 Sensor. The process of preparing stably transfected MDCK cell lines expressing a Grx1-roGFP2 sensor with lentiviral vectors is schematically illustrated in Figure 2a. The target gene (Grx1-roGFP2) was obtained by fusing roGFP2 with the human Grx1 gene. The target gene (Grx1-roGFP2) was cloned into the lentiviral vector pLV puro and then infected with MDCK cells. Stable MDCK cell lines were screened using puromycin. All primer sequences used in this study are listed in Table S2. The expression of Grx1-roGFP2 mRNA was quantified by real-time PCR, and clone 4 was selected for subsequent studies due to its highest expression level of Grx1-roGFP2 mRNA among engineered MDCK cells (Figure 2b). Furthermore, fluorescence imaging was performed on the engineered MDCK cells expressing the Grx1-roGFP2 sensor. As shown in Figure 2c, in the absence of any oxidative stress inducer, a robust green fluorescence signal (reduced state, 488 nm excitation wavelength) was observed in the cytoplasm, while almost no red fluorescence signal (oxidized state, 405 nm excitation wavelength) was detected. Thus, an engineered MDCK cell line expressing the Grx1-roGFP2 sensor for real-time monitoring of redox equilibrium was successfully constructed.

3.4. Performance Evaluation of the Grx1-roGFP2 Sensor. To investigate the redox-sensing performance of the developed Grx1-roGFP2 sensor, MDCK cells expressing the engineered sensor were subjected to a 30-μM H_2O_2 challenge and conducted a continuous 24-h monitoring. The engineered MDCK cells were excited with 405 nm and 488 nm lasers, and imaging was recorded with emission in the green channel (~520 nm). Three replicate experiments were conducted. Figure 3a,b illustrates the imaging sequence of a representative ROI at multiple time points, while additional images were presented in Supplementary Figure S2. The results showed that the two fluorescence signals generated by the biosensor had obvious dynamic changes over time (Figure 3a,b). The excitation spectra of Grx1-roGFP2 in reducing and oxidizing states are shown in Figure 3c. Specifically, the fluorescence intensity corresponding to the reduced state (green) showed a

https://doi.org/10.1021/acsomega.5c00774
ACS Omega 2025, 10, 15587−15597

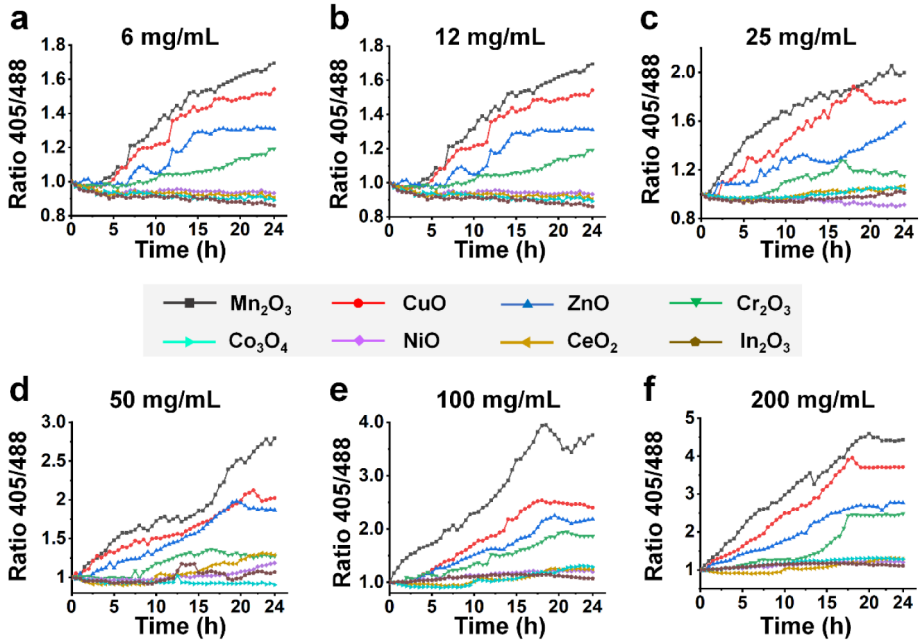

Figure 4. Response of Grx1-roGFP sensor to various MOx nanoparticles. The engineered MDCK cells expressing Grx1-roGFP sensor were exposed to eight different MOx nanoparticles with a range of concentrations for desired time: (a) 6, (b) 12, (c) 25, (d) 50, (e) 100, and (f) 200 mg/mL. MOx nanoparticle-induced changes in oxidation levels were assessed by calculating the ratio of fluorescence intensities excited at 405/488 nm. The fluorescence values prior to ratio calculation were normalized relative to the initial fluorescence values at the 0 min time point for each sample.

gradual decrease, whereas that of the oxidized state (red) was gradually enhanced (Figure 3d). Furthermore, the fluorescence ratio of 405/488 nm was plotted to quantitatively reflect the oxidative environment fluctuations in MDCK cells after H_2O_2 treatment. The results (Figure 3e) showed that H_2O_2-induced oxidative stress led to an initial surge of the fluorescence ratio intensity within 30 min, followed by a subsequent attenuation in the rate of increase, and finally culminated a relatively stable plateau at 10 h. These findings indicated that the constructed sensor can respond rapidly to H_2O_2-induced oxidative stress with considerable sensitivity and temporal resolution.

Meanwhile, to compare the performance of the developed biosensor with that of traditional fluorescent probes, wild-type MDCK cells were treated with the same concentration of H_2O_2 at different time intervals, and their fluorescence intensity was measured using a CM-H_2DCFDA assay. Unlike the sensitive performance of the Grx1-roGFP2 sensor, the fluorescence intensity detected by the CM-H_2DCFDA assay did not deviate significantly from that of the blank control, despite showing an increasing trend (Figure 3f). The above results highlighted the superiority of our developed Grx1-roGFP2 system over traditional CM-H_2DCFDA methods in terms of sensitivity and real-time dynamic monitoring of cellular redox homeostasis.

3.5. Application of the Grx1-roGFP2 Sensor for MOx-Induced Oxidative Stress. For the evaluation of MOx nanoparticle-induced oxidative stress with the Grx1-roGFP2 sensor, the engineered MDCK cells were treated with eight representative MOx nanoparticles (Mn_2O_3, CuO, ZnO, Cr_2O_3, Co_3O_4, NiO, CeO_2, and In_2O_3) across a spectrum of concentrations and at various time points. Representative snapshots of the reduced Grx1-roGFP2 and oxidized Grx1-roGFP2 at each time point are provided in Figures S3−S8. The ratio of the 405/488 nm fluorescence intensity was plotted to quantitatively reflect the fluctuating oxidative environment within the engineered MDCK cells (Figure 4a−f). Overall, MOx nanoparticle-induced oxidation levels showed a positive correlation with the concentration and actuation duration of MOx nanoparticles. The differences in oxidation levels resulted from MOx nanoparticles were closely related to their band gap energies and solubility. Specifically, MOx nanoparticles with band gap energies overlapping biological redox potential (Mn_2O_3, Cr_2O_3, and Co_3O_4) led to a rapid increase in the 405/488 fluorescence ratio; MOx nanoparticles with band gap energies not overlapping biological redox potential (NiO, CeO_2, In_2O_3) resulted in a limited increase in the 405/488 fluorescence ratio; MOx nanoparticles (CuO and ZnO) with high solvation activity (capable of releasing metal ions) also significantly improved the 405/488 fluorescence ratio. These findings were largely in line with the current toxicological studies regarding MOx nanoparticles, which generate oxygen radicals and oxidative stress.

Notably, the developed Grx1-roGFP2 sensor, with its sensitive and dynamic monitoring pattern, provided us with more detailed information not available from previous research methods. The fluorescence-ratio signal depicts a characteristic map of oxidative stress induced by each MOx nanoparticle. The results (Figure 4a−f) showed that the fluorescence-ratio plots generated by MOx nanoparticles were either parabolic, concave, or close to a straight line, which were closely related to the MOx nanoparticles' concentrations and action duration. Presented in ascending order of the degree of induced oxidative stress: the oxidation state change induced by Mn_2O_3 was closer to a linearly ascending mode, with the amplitude being most pronounced among all MOx nanoparticles. In contrast, the Cr_2O_3-induced changes demonstrated a significant delay, and the amplitude was significantly lower than that of Mn_2O_3 nanoparticles. The fluorescence ratio induced by CuO and ZnO (which can release metal ions) showed a certain degree of attenuation after increasing beyond

https://doi.org/10.1021/acsomega.5c00774
ACS Omega 2025, 10, 15587−15597

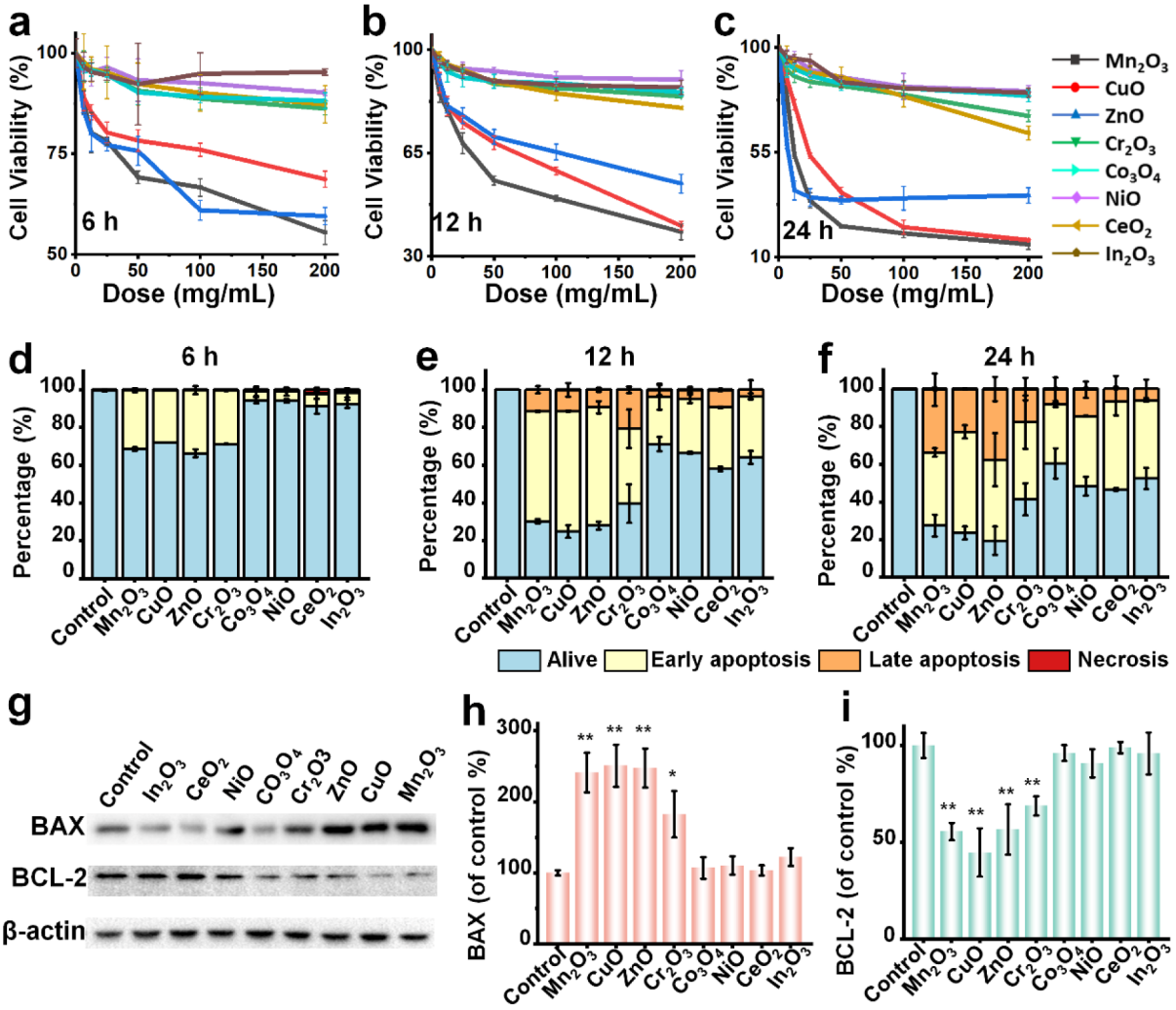

Figure 5. Cellular toxicity testing of MOx nanoparticles in MDCK cells. The MDCK cells were treated with MOx nanoparticles at concentrations ranging from 0 to 200 mg/mL for 6, 12, and 24 h. (a−c) MTS assay for cell viability. (d−f) Quantitative analysis of apoptosis/necrosis in MDCK cells after exposure to different concentrations of MOx nanoparticles for 6, 12, and 24 h; these analyses correspond to the flow cytometry data of Figures S8−S10. (g−i) Western blot analysis was performed to determine the expression levels of the pro-apoptotic protein BAX and the antiapoptotic protein BCL-2. Results are depicted as mean ± SD, $n = 3$, $^{*}p < 0.05$, and $^{**}p < 0.01$, compared to the control group.

a certain level. Co_3O_4 nanoparticles did not show the anticipated high level despite their band gap energy coinciding with the cellular redox potential, implying possible toxicological mechanisms apart from oxidative stress. Unexpectedly, CeO_2 and In_2O_3 existed at maximum induced concentrations of 50 and 100 mg/mL, respectively. All materials exhibited a plateau after prolonged exposure to high concentrations, indicating a maximum oxidation level induced by MOx nanoparticles. The dynamic characteristics provided by the fluorescence-ratio plot implied different mechanisms by which different MOx nanoparticles induced cellular oxidative stress. In summary, the developed Grx1-roGFP2 sensor was fully capable of sensitive, dynamic, and quantitative detection of MOx nanoparticle-induced changes in cellular redox homeostasis.

3.6. Cellular Toxicity Testing Associated with Oxidation Levels. Cell viability and apoptosis, as downstream events of MOx-induced oxidative stress, were further investigated. First, after treating MDCK cells with MOx nanoparticles at different doses (0−200 mg/mL) for 6, 12, and 24 h, cell viability was assessed using the MTS assay. The results Figure 5a−c showed that Mn_2O_3, CuO, and ZnO significantly reduced cell viability, whereas other MOx nanoparticles had less effect. The magnitude of the MOx nanoparticle-induced decrease in cell viability was consistent with their ability to increase cellular oxidation levels. Furthermore, flow cytometry combined with Annexin V/Propidium Iodide (PI) double staining was used to assess the cell apoptosis response to various MOx nanoparticles (Figures S9−S11 and Figure 5d−f). MDCK cells were treated with eight MOx nanoparticles at a concentration of 100 mg/mL for 6, 12, and 24 h. Generally, the proportions of apoptosis (both early and late apoptosis) caused by the MOx nanoparticles were consistent with their ability to elevate cellular oxidation levels. The apoptosis rate caused by four MOx nanoparticles (Mn_2O_3, ZnO, CuO, and Cr_2O_3) was particularly significant, regardless of treatment for 6 h (Figure 5d), 12 h (Figure 5e), and 24 h (Figure 5f). Corresponding to the high 405/488 nm fluorescence ratio (Figure 4e, 100 mg/mL MOx), after 24 h, total apoptosis increased to 85.7% for ZnO, 78.7% for CuO, 76.5% for Mn_2O_3, and 52.6% for Cr_2O_3 (Figure 4f). Notably, Mn_2O_3, which caused the highest cellular oxidation level, did

https://doi.org/10.1021/acsomega.5c00774
ACS Omega 2025, 10, 15587−15597

not lead to the greatest apoptosis, suggesting a complex toxicological mechanism outside of oxidative stress. As expected, ZnO and CuO (capable of releasing metal ions) induced remarkable apoptotic rates. The MTS assay and the Annexin V/PI apoptosis assay assess distinct biological processes, with the former reflecting cellular metabolic activity and the latter being specifically designed to detect apoptosis and its stages. Consequently, minor divergences were observed between the two measurements for certain MOx materials.

Correspondingly, western blot (WB) analysis was employed to assess the expression levels of the pro-apoptotic protein BAX and the antiapoptotic protein BCL-2. Following 24-h exposure to 100 mg/mL of eight MOx nanoparticles, WB images (Figure 5g) and the corresponding densitometric analysis (Figure 5h for BAX and Figure 5i for BCL-2) showed that Mn_2O_3, CuO, ZnO, and Cr_2O_3 notably upregulated BAX expression and concurrently downregulated BCL-2 expression, which were consistent with these MOx-induced apoptosis trends. The above results indicate that the Grx1-roGFP sensor constructed in this study has great potential for application as a promising cellular assessment model for nanotoxicology.

4. DISCUSSION

Over the past decades, nanomaterials have been widely used in medical, cosmetic, food, and engineering fields.[39−41] With the increasing use of nanomaterials, their toxicological effects on the human body and the environment have gradually attracted people's attention.[1−3] Previous studies have demonstrated that the induction of oxidative stress by MOx nanoparticles constitutes one of the main mechanisms by which they damage organisms. Thus, MOx nanoparticles are chosen as the analysis targets in this study. MOx nanoparticles enter cells and induce cytotoxicity through the accumulation of oxygen radicals and alteration of the antioxidant system. Oxygen radicals are associated with many diseases, causing cell and tissue damage by inducing DNA denaturation, protein oxidation, and the release of pro-inflammatory cytokines.[42] Considering that oxygen radicals are characterized by a short lifespan, rapid conversion rate, high reactivity, and low concentration, the development of probes capable of real-time in situ monitoring is of great significance for studying the biological functions of oxygen radicals. However, the relevant probes and auxiliary methods developed so far suffer from problems such as destructive invasion, imposed oxidative damage, background interference, insufficient tissue penetration, toxicity, and complex operation, which limit their application in nanotoxicology studies. For this work, we developed a redox-sensitive GFP sensing strategy with the aim of establishing an efficient oxidative stress monitoring system for nanotoxicological assessments.

In this study, we constructed a Grx1-roGFP2 fusion protein expressed in MDCK cells, in which Grx1 catalyzes the equilibrium between glutathione and roGFP2, thereby enabling real-time monitoring of changes in cellular redox potential. By plotting the real-time fluorescence ratio signal graph, the response of the sensor to H_2O_2-induced oxidative stress can be observed, demonstrating outstanding sensitivity and resolution in monitoring the subtle fluctuations of intracellular redox equilibrium (Figure 3c). In contrast, the conventional CM-H_2DCFDA method lacks sensitivity because it fails to detect changes in intracellular redox equilibrium at most time points (Figure 3d). Although CM-H_2DCFDA remains a widely employed fluorescent probe for ROS detection, its inherent limitations manifest as compromised sensitivity, nonspecific signal interference, and dependence on esterase-mediated signal transduction, coupled with fluorophore quenching artifacts. To address the limitations of CM-H_2DCFDA, an optimization strategy that integrates multiplatform analysis techniques, including mass spectrometry and flow cytometry, can enhance the accuracy and sensitivity of ROS detection. However, this approach also introduces additional complexity to the analysis. On this basis, the developed Grx1-roGFP2 sensor is subjected to tests with eight representative MOx nanoparticles having different band gap energies and metal ion release profiles.

The criteria for the selection of MOx nanoparticles are as follows: ZnO and CuO are capable of releasing metal ions in large quantities (metal ion solubility of more than 13.05%), and previous studies have confirmed that dissociated metal ions catalyze the production of H_2O_2 and hydroxyl radicals (OH), which has led to ZnO and CuO being categorized as highly toxic nanoparticles. In contrast, other less soluble MOx nanoparticles can be classified and ranked based on their bandgap energies.[14,15] Mn_2O_3, Cr_2O_3, and Co_3O_4, whose bandgap energy overlaps with the cellular redox potential range (−4.12 to −4.84 eV), can interact more effectively with cellular redox systems, thereby endowing them with high toxicity. Whereas MOx nanoparticles with band gap energies located outside the cellular redox potential interval (NiO, CeO_2 and In_2O_3) are served as controls for the low toxicity category. Impressively, the developed Grx1-roGFP2 sensor demonstrates outstanding performance in monitoring changes in the intracellular redox equilibrium triggered by MOx nanoparticles. The measurement outcomes of the Grx1-roGFP2 sensor not only revalidate previous conclusions but also provide more detailed information through the plotted fluorescence-ratio signal, which is inaccessible through previous research approaches. Figure S12 illustrates a schematic representation of the parameters in the fluorescence ratio curve that signify the ROS response. This encompasses the generated stress intensity (curve slope), the characteristics (curve shape), degree (curve plateau), and the accumulation of oxygen radicals (curve area integral), reflecting the unique pattern of oxidative stress induced by different MOx nanoparticles (Figure 4a−f). These patterns facilitate the elucidation of subsequent nanotoxicological effects and underlying mechanisms, such as cell viability and apoptosis induced by MOx nanoparticles (Figure 5).

Encouragingly, the fusion strategy of roGFP with interest proteins is extremely scalable, resulting in the generation of diversified genetically encoded reporters for oxidative stress that have been designed and applied in different model systems.[26] The antioxidant system of an organism is a complex network system composed of antioxidant enzymes and/or nonenzymatic antioxidants working together to resist potential oxidative damage.[43] The thiol-dependent antioxidant system is a powerful antioxidant defense system against potential oxidative threats, mainly composed of glutathione (GSH), thioredoxins (Trxs), glutaredoxins (Grxs), and peroxiredoxins (Prxs).[44,45] The fusion of roGFP with Trxs, Grxs, and Prxs, key enzymes of the sulfhydryl-dependent antioxidant system, has been successfully developed and applied as oxidative stress monitoring probes.[26,29−33,46,47] Similarly, based on the importance of H_2O_2 as a central molecule in maintaining redox homeostasis, roGFP variants have been fused to H_2O_2-specific responsive enzymes, which have been demonstrated to

https://doi.org/10.1021/acsomega.5c00774
ACS Omega 2025, 10, 15587−15597

monitor intracellular H_2O_2 levels *in vivo* with unprecedented sensitivity.[26,34] The development of these engineering probes is of great significance for in-depth clarification of the mechanism of nanooxidative damage and for taking effective intervention measures.

Furthermore, it is an incontrovertible fact that the interaction process between nanomaterials and the human body is highly intricate.[48,49] Nanomaterials can enter the human circulation through multiple exposure routes, involving skin, respiratory system, digestive system, or direct intravenous injection.[50,51] Different exposure pathways determine the specific tissue distribution and differentiated toxicological effects of the nanomaterials. After long-term practice, scientists have found that the interactions between nanoparticles and organisms are affected by a variety of factors, such as particle size, surface charge, shape, and surface coatings, forming a complex pattern of nanoparticle-induced oxygen radicals and oxidative stress.[9−11] Encouragingly, advances in gene editing technology allow for the easy construction of roGFP fusion sensors in tissue and cell interests, providing the required information on oxygen radicals and oxidative stress. Consequently, our proposed genetically engineered sensing strategy, which fuses roGFP with sulfhydryl-dependent antioxidant enzymes, is a noninvasive sensing technology with excellent sensitivity and resolution in real-time monitoring of intracellular redox homeostasis fluctuations, emerging as a potent tool for nanotoxicological studies with promising applications.

5. CONCLUSION

In summary, the developed Grx1-roGFP2 sensor can dynamically respond to fluctuations in cellular oxidative homeostasis triggered by MOxx nanoparticle exposure. The morphology of the fluorescence-ratio curve output from the sensor, including shape, slope, highest plateau, and area integral, dynamically portrays the specific patterns of MOx-induced oxidative stress, providing key information for subsequent toxicological effect assessment and potential mechanism studies. Gene-editing-based sensing strategies hold significant promise in nanotoxicity research. Multidimensional innovations, such as enhanced multimodal detection, improved spatiotemporal resolution, optimized dynamic monitoring, and integration with artificial intelligence (AI) or high-throughput screening, are poised to substantially advance the accuracy and safety assessment of nanotechnology systems, thereby supporting nanomaterial development and industrialization.

■ ASSOCIATED CONTENT

Data Availability Statement

The data underlying this study are available within the manuscript and its Supporting Information files.

Supporting Information

The Supporting Information is available free of charge at https://pubs.acs.org/doi/10.1021/acsomega.5c00774.

TEM characterization of MOx; surface potential of MOx; PCR primer sequences; dynamic imaging of MOx nanoparticle-induced oxidative stress; flow cytometry analysis for apoptosis/necrosis; and Supporting Figures S1−S12 and Tables S1−S2 (PDF)

■ AUTHOR INFORMATION

Corresponding Authors

Xiaonan Li − *Department of Information Engineering, Shijiazhuang Institute of Railway Technology, Shijiazhuang, Hebei Province 050041, P. R. China*; Email: adpressed@163.com

Na Wang − *College of Pharmacy, Hebei Medical University, Shijiazhuang, Hebei Province 050017, P.R. China*; Email: 18200975@hebmu.edu.cn

Authors

Yizhu Wang − *China Medical University-The Queen's University of Belfast Joint College (CQC), China Medical University, Shenyang, Liaoning Province 110122, P.R. China*

Rui Ju − *Research Institute of Biomedical and Advanced Materials, College of Life and Health, Dalian University, Dalian, Liaoning Province 116622, P. R. China*; orcid.org/0009-0004-8573-021X

Yan Fu − *College of Pharmacy, Hebei Medical University, Shijiazhuang, Hebei Province 050017, P.R. China*

Fengqi Zhang − *College of Pharmacy, Hebei Medical University, Shijiazhuang, Hebei Province 050017, P.R. China*

Ziyue Yin − *College of Pharmacy, Hebei Medical University, Shijiazhuang, Hebei Province 050017, P.R. China*

Mengyuan Lv − *Research Institute of Biomedical and Advanced Materials, College of Life and Health, Dalian University, Dalian, Liaoning Province 116622, P. R. China*

Yanbo Zhu − *College of Pharmacy, Hebei Medical University, Shijiazhuang, Hebei Province 050017, P.R. China; Department of Rehabilitation Medicine, The Third Hospital of Hebei Medical University, Shijiazhuang 050051, P.R. China*

Zhiqiang Song − *College of Pharmacy, Hebei Medical University, Shijiazhuang, Hebei Province 050017, P.R. China*

Complete contact information is available at: https://pubs.acs.org/10.1021/acsomega.5c00774

Author Contributions

#Y.W.,R.J., and Y.F. contributed equally to this work. Y.W., R.J., and Y.F. performed most of the experiments. Y.W. and N.W. wrote the manuscript. F.Z. and Z.Y. constructed the fusion protein sensor. M.L. performed molecular experiments. Y.Z. and Z.S. performed sensing analysis. X.L. analyzed the data. N.W. supervised the project. All authors discussed the results and commented on the manuscript.

Notes

The authors declare no competing financial interest.

■ ACKNOWLEDGMENTS

Financial support is provided by the Natural Science Foundation of Hebei Province (No. H2022206507 and H2022206456), the Hebei Province High School Science and Technology Research Project (2024ZJJGGC23), and the Subject Construction Project of Dalian University (DLUXK-2022-ZD-002).

■ REFERENCES

(1) Yang, W.; Wang, L.; Mettenbrink, E. M.; DeAngelis, P. L.; Wilhelm, S. Nanoparticle Toxicology. *Annu. Rev. Pharmacol. Toxicol.* **2021**, *61* (2021), 269−289.

(2) Najahi-Missaoui, W.; Arnold, R. D.; Cummings, B. S. Safe Nanoparticles: Are We There Yet? *Int. J. Mol. Sci.* **2021**, *22* (1), 385.

(3) Khan, I.; Saeed, K.; Khan, I. Nanoparticles: Properties, applications and toxicities. *Arab. J. Chem.* **2019**, *12* (7), 908−931.
(4) Truong, T. T.; Mondal, S.; Doan, V. H. M.; Tak, S.; Choi, J.; Oh, H.; Nguyen, T. D.; Misra, M.; Lee, B.; Oh, J. Precision-engineered metal and metal-oxide nanoparticles for biomedical imaging and healthcare applications. *Adv. Colloid Interface Sci.* **2024**, *332*, 103263.
(5) Chouke, P. B.; Shrirame, T.; Potbhare, A. K.; Mondal, A.; Chaudhary, A. R.; Mondal, S.; Thakare, S. R.; Nepovimova, E.; Valis, M.; Kuca, K.; Sharma, R.; Chaudhary, R. G. Bioinspired metal/metal oxide nanoparticles: A road map to potential applications. *Mater. Today Adv.* **2022**, *16*, 100314.
(6) Sengul, A. B.; Asmatulu, E. Toxicity of metal and metal oxide nanoparticles: a review. *Environ. Chem. Lett.* **2020**, *18* (5), 1659−1683.
(7) Kessler, A.; Hedberg, J.; Blomberg, E.; Odnevall, I. Reactive Oxygen Species Formed by Metal and Metal Oxide Nanoparticles in Physiological Media-A Review of Reactions of Importance to Nanotoxicity and Proposal for Categorization. *Nanomaterials* **2022**, *12* (11), 1922.
(8) Bi, J.; Mo, C.; Li, S.; Huang, M.; Lin, Y.; Yuan, P.; Liu, Z.; Jia, B.; Xu, S. Immunotoxicity of metal and metal oxide nanoparticles: from toxic mechanisms to metabolism and outcomes. *Biomater. Sci.* **2023**, *11* (12), 4151−4183.
(9) Ali, M. What function of nanoparticles is the primary factor for their hyper-toxicity? *Adv. Colloid Interface Sci.* **2023**, *314*, 102881.
(10) Joudeh, N.; Linke, D. Nanoparticle classification, physicochemical properties, characterization, and applications: a comprehensive review for biologists. *J. Nanobiotechnol.* **2022**, *20* (1), 262.
(11) Abbasi, R.; Shineh, G.; Mobaraki, M.; Doughty, S.; Tayebi, L. Structural parameters of nanoparticles affecting their toxicity for biomedical applications: a review. *J. Nanopart. Res.* **2023**, *25* (3), 43.
(12) Martin, A.; Sarkar, A. Overview on biological implications of metal oxide nanoparticle exposure to human alveolar A549 cell line. *Nanotoxicology* **2017**, *11* (6), 713−724.
(13) Mirshafiee, V.; Sun, B.; Chang, C. H.; Liao, Y.-P.; Jiang, W.; Jiang, J.; Liu, X.; Wang, X.; Xia, T.; Nel, A. E. Toxicological Profiling of Metal Oxide Nanoparticles in Liver Context Reveals Pyroptosis in Kupffer Cells and Macrophages versus Apoptosis in Hepatocytes. *ACS Nano* **2018**, *12* (4), 3836−3852.
(14) Burello, E.; Worth, A. P. A theoretical framework for predicting the oxidative stress potential of oxide nanoparticles. *Nanotoxicology* **2011**, *5* (2), 228−235.
(15) Zhang, H. Y.; Ji, Z. X.; Xia, T.; Meng, H.; Low-Kam, C.; Liu, R.; Pokhrel, S.; Lin, S. J.; Wang, X.; Liao, Y. P.; Wang, M. Y.; Li, L. J.; Rallo, R.; Damoiseaux, R.; Telesca, D.; Mädler, L.; Cohen, Y.; Zink, J. I.; Nel, A. E. Use of Metal Oxide Nanoparticle Band Gap To Develop a Predictive Paradigm for Oxidative Stress and Acute Pulmonary Inflammation. *ACS Nano* **2012**, *6* (5), 4349−4368.
(16) Wang, D. L.; Lin, Z. F.; Wang, T.; Yao, Z. F.; Qin, M. N.; Zheng, S. R.; Lu, W. Where does the toxicity of metal oxide nanoparticles come from: The nanoparticles, the ions, or a combination of both? *J. Hazard. Mater.* **2016**, *308*, 328−334.
(17) Avramescu, M.-L.; Chenier, M.; Beauchemin, S.; Rasmussen, P. Dissolution Behaviour of Metal-Oxide Nanomaterials in Various Biological Media. *Nanomaterials* **2023**, *13* (1), 26.
(18) Liu, H.; Lai, W.; Liu, X.; Yang, H.; Fang, Y.; Tian, L.; Li, K.; Nie, H.; Zhang, W.; Shi, Y.; Bian, L.; Ding, S.; Yan, J.; Lin, B.; Xi, Z. Exposure to copper oxide nanoparticles triggers oxidative stress and endoplasmic reticulum (ER)-stress induced toxicology and apoptosis in male rat liver and BRL-3A cell. *J. Hazard. Mater.* **2021**, *401*, 123349.
(19) Fujihara, J.; Nishimoto, N. Review of Zinc Oxide Nanoparticles: Toxicokinetics, Tissue Distribution for Various Exposure Routes, Toxicological Effects, Toxicity Mechanism in Mammals, and an Approach for Toxicity Reduction. *Biol. Trace Elem. Res.* **2024**, *202* (1), 9−23.
(20) Munteanu, I. G.; Apetrei, C. Analytical Methods Used in Determining Antioxidant Activity: A Review. *Int. J. Mol. Sci.* **2021**, *22* (7), 3380.
(21) Wang, J.; Wang, S. Reactive species in advanced oxidation processes: Formation, identification and reaction mechanism. *Chem. Eng. J.* **2020**, *401*, 126158.
(22) Wu, L.; Sedgwick, A. C.; Sun, X.; Bull, S. D.; He, X.-P.; James, T. D. Reaction-Based Fluorescent Probes for the Detection and Imaging of Reactive Oxygen, Nitrogen, and Sulfur Species. *Acc. Chem. Res.* **2019**, *52* (9), 2582−2597.
(23) Zhang, Y. F.; Dai, M. H.; Yuan, Z. H. Methods for the detection of reactive oxygen species. *Anal. Methods* **2018**, *10* (38), 4625−4638.
(24) Chen, X.; Wang, F.; Hyun, J. Y.; Wei, T.; Qiang, J.; Ren, X.; Shin, I.; Yoon, J. Recent progress in the development of fluorescent, luminescent and colorimetric probes for detection of reactive oxygen and nitrogen species. *Chem. Soc. Rev.* **2016**, *45* (10), 2976−3016.
(25) Morgan, B.; Sobotta, M. C.; Dick, T. P. Measuring EGSH and H2O2 with roGFP2-based redox probes. *Free Radical Bio. Med.* **2011**, *51* (11), 1943−1951.
(26) Geissel, F.; Lang, L.; Husemann, B.; Morgan, B.; Deponte, M. Deciphering the mechanism of glutaredoxin-catalyzed roGFP2 redox sensing reveals a ternary complex with glutathione for protein disulfide reduction. *Nat. Commun.* **2024**, *15* (1), 1733.
(27) Sies, H.; Mailloux, R. J.; Jakob, U. Fundamentals of redox regulation in biology. *Nat. Rev. Mol. Cell Biol.* **2024**, *25* (9), 701−719.
(28) Hong, Y.; Boiti, A.; Vallone, D.; Foulkes, N. S. Reactive Oxygen Species Signaling and Oxidative Stress: Transcriptional Regulation and Evolution. *Antioxidants* **2024**, *13* (3), 312.
(29) Arnaud, D.; Deeks, M. J.; Smirnoff, N. Organelle-targeted biosensors reveal distinct oxidative events during pattern-triggered immune responses. *Plant Physiol.* **2023**, *191* (4), 2551−2569.
(30) Heimsch, K. C.; Gertzen, C. G. W.; Schuh, A. K.; Nietzel, T.; Rahlfs, S.; Przyborski, J. M.; Gohlke, H.; Schwarzlaender, M.; Becker, K.; Fritz-Wolf, K. Structure and Function of Redox-Sensitive Superfolder Green Fluorescent Protein Variant. *Antioxid. Redox Signaling* **2022**, *37* (1−3), 1−18.
(31) Jorgensen, A. N.; Rashdan, N. A.; Rao, K. N. S.; Delgadillo, L. F.; Kolluru, G. K.; Krzywanski, D. M.; Pattillo, C. B.; Kevil, C. G.; Nam, H. W. Neurogranin expression regulates mitochondrial function and redox balance in endothelial cells. *Redox Biol.* **2024**, *70*, 103085.
(32) Molinari, P. E.; Krapp, A. R.; Weiner, A.; Beyer, H. M.; Kondadi, A. K.; Blomeier, T.; López, M.; Bustos-Sanmamed, P.; Tevere, E.; Weber, W.; et al. NERNST: a genetically-encoded ratiometric non-destructive sensing tool to estimate NADP(H) redox status in bacterial, plant and animal systems. *Nat. Commun.* **2023**, *14* (1), 3277.
(33) Balta, E.; Hardt, R.; Liang, J.; Kirchgessner, H.; Orlik, C.; Jahraus, B.; Hillmer, S.; Meuer, S.; Hübner, K.; Wabnitz, G. H.; et al. Spatial oxidation of L-plastin downmodulates actin-based functions of tumor cells. *Nat. Commun.* **2019**, *10* (1), 4073.
(34) Nietzel, T.; Elsässer, M.; Ruberti, C.; Steinbeck, J.; Ugalde, J. M.; Fuchs, P.; Wagner, S.; Ostermann, L.; Moseler, A.; Lemke, P.; Fricker, M. D.; Müller-Schüssele, S. J.; Moerschbacher, B. M.; Costa, A.; Meyer, A. J.; Schwarzländer, M. The fluorescent protein sensor roGFP2-Orp1 monitors in vivo H2O2 and thiol redox integration and elucidates intracellular H2O2 dynamics during elicitor-induced oxidative burst in Arabidopsis. *New Phytol.* **2019**, *221* (3), 1649−1664.
(35) Bray, M.-A.; Singh, S.; Han, H.; Davis, C. T.; Borgeson, B.; Hartland, C.; Kost-Alimova, M.; Gustafsdottir, S. M.; Gibson, C. C.; Carpenter, A. E. Cell Painting, a high-content image-based assay for morphological profiling using multiplexed fluorescent dyes. *Nat. Protoc.* **2016**, *11* (9), 1757−1774.
(36) Belmas, T.; Liesa, M.; Shum, M. Quantifying mitochondrial redox and bilirubin content in intact primary hepatocytes of obese mice using fluorescent reporters. *STAR Protoc.* **2023**, *4* (3), 102408−102408.
(37) Lee, Y.; McAllister, K.; Lee, H. R.; Jung, S.; Murphy, F. Evaluation of a bioprinted 3D airway tissue model for toxicity testing of nanomaterials; Pathway to integration into a tiered testing strategy for hazard assessment to support safety-by-design. *Nano Today* **2025**, *61*, 102655.

https://doi.org/10.1021/acsomega.5c00774
ACS Omega 2025, 10, 15587−15597

(38) Battistini, B.; Lulli, D.; Bocca, B.; Carbone, M. L.; Ramondino, C.; Caimi, S.; Capone, A.; Nicodemi, E. M.; Dellambra, E.; De Angelis, I.; Failla, C. M. Tattoo Ink Metal Nanoparticles: Assessment of Toxicity In Vitro and with a Novel Human Ex Vivo Model. *Nanomaterials* **2025**, *15* (4), 270.
(39) Mitchell, M. J.; Billingsley, M. M.; Haley, R. M.; Wechsler, M. E.; Peppas, N. A.; Langer, R. Engineering precision nanoparticles for drug delivery. *Nat. Rev. Drug Discovery* **2021**, *20* (2), 101−124.
(40) Kirtane, A. R.; Verma, M.; Karandikar, P.; Furin, J.; Langer, R.; Traverso, G. Nanotechnology approaches for global infectious diseases. *Nat. Nanotechnol.* **2021**, *16* (4), 369−384.
(41) Lowry, G. V.; Avellan, A.; Gilbertson, L. M. Opportunities and challenges for nanotechnology in the agri-tech revolution. *Nat. Nanotechnol.* **2019**, *14* (6), 517−522.
(42) Juan, C. A.; Perez de la Lastra, J. M.; Plou, F. J.; Perez-Lebena, E. The Chemistry of Reactive Oxygen Species (ROS) Revisited: Outlining Their Role in Biological Macromolecules (DNA, Lipids and Proteins) and Induced Pathologies. *Int. J. Mol. Sci.* **2021**, *22* (9), 4642.
(43) Jomova, K.; Raptova, R.; Alomar, S. Y.; Alwasel, S. H.; Nepovimova, E.; Kuca, K.; Valko, M. Reactive oxygen species, toxicity, oxidative stress, and antioxidants: chronic diseases and aging. *Arch. Toxicol.* **2023**, *97* (10), 2499−2574.
(44) Andreadou, I.; Efentakis, P.; Frenis, K.; Daiber, A.; Schulz, R. Thiol-based redox-active proteins as cardioprotective therapeutic agents in cardiovascular diseases. *Basic Res. Cardiol.* **2021**, *116* (1), 44.
(45) Ulrich, K.; Jakob, U. The role of thiols in antioxidant systems. *Free Radical Bio. Med.* **2019**, *140*, 14−27.
(46) Castro, H.; Rocha, M. I.; Duarte, M.; Vilurbina, J.; Gomes-Alves, A. G.; Leao, T.; Dias, F.; Morgan, B.; Deponte, M.; Tomás, A. M. The cytosolic hyperoxidation-sensitive and -robust Leishmania peroxiredoxins cPRX1 and cPRX2 are both dispensable for parasite infectivity. *Redox Biol.* **2024**, *71*, 103122.
(47) Collado-Arenal, A. M.; Exposito-Rodriguez, M.; Mullineaux, P. M.; Olmedilla, A.; Romero-Puertas, M. C.; Sandalio, L. M. Cadmium exposure induced light/dark- and time-dependent redox changes at subcellular level in Arabidopsis plants. *J. Hazard. Mater.* **2024**, *477*, 135164.
(48) Ji, Y. X.; Wang, Y. Q.; Wang, X. Y.; Lv, C. J.; Zhou, Q. F.; Jiang, G. B.; Yan, B.; Chen, L. X. Beyond the promise: Exploring the complex interactions of nanoparticles within biological systems. *J. Hazard. Mater.* **2024**, *468*, 133800.
(49) Zhang, Y.; Bai, Y. H.; Jia, J. B.; Gao, N. N.; Li, Y.; Zhang, R. N.; Jiang, G. B.; Yan, B. Perturbation of physiological systems by nanoparticles. *Chem. Soc. Rev.* **2014**, *43* (10), 3762−3809.
(50) Peng, Y.; Yang, Z.; Sun, H.; Li, J.; Lan, X.; Liu, S. Nanomaterials in Medicine: Understanding Cellular Uptake, Localization, and Retention for Enhanced Disease Diagnosis and Therapy. *Aging Dis.* **2025**, *16* (1), 168−208.
(51) Malakar, A.; Kanel, S. R.; Ray, C.; Snow, D. D.; Nadagouda, M. N. Nanomaterials in the environment, human exposure pathway, and health effects: A review. *Sci. Total Environ.* **2021**, *759*, 143470.

https://doi.org/10.1021/acsomega.5c00774
ACS Omega 2025, 10, 15587−15597